UC San Diego
UC San Diego Previously Published Works

Title

Probing the densification mechanisms during flash sintering of ZnO

Permalink

Authors

Zhang, Yuanyao
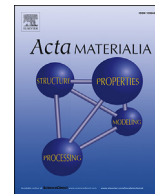Nie, Jiuyuan
Chan, Jonathan Michael
et al.

Publication Date

DOI

Peer reviewed

Full length article

Liquid-like grain boundary complexion and sub-eutectic activated sintering in CuO-doped TiO$_2$

Jiuyuan Nie, Jonathan M. Chan, Mingde Qin, Naixie Zhou, Jian Luo[*]

Department of NanoEngineering, University of California, San Diego, La Jolla, CA 92093, USA

ABSTRACT

The eutectic temperature and composition of the TiO$_2$-CuO system were carefully measured to be 1010 ± 10 °C and 83CuO:17TiO$_2$, respectively. Subsequently, a TiO$_2$-CuO phase diagram was computed, representing a correction and major improvement from the phase diagram available in literature. Dilatometry measurements and isothermal sintering experiments unequivocally demonstrated the activated (enhanced) sintering of TiO$_2$ with the addition of CuO, occurring at as low as >300 °C below the eutectic temperature. High resolution transmission electron microscopy (HRTEM) characterization of water-quenched specimens revealed the formation of nanometer-thick, liquid-like, intergranular films (IGFs), a type of grain boundary (GB) complexion (a.k.a. 2-D interfacial phase), concurrently with accelerated densification and well below the bulk eutectic temperature. Consequently, activated sintering is explained from the enhanced mass transport in this premelting-like complexion. An interfacial thermodynamic model was used to quantitatively explain and justify the stabilization of liquid-like IGFs below the eutectic temperature and the temperature-dependent IGF thicknesses measured by HRTEM. A GB λ diagram was computed, for the first time for a ceramic system, to represent the thermodynamic tendency for general GBs in CuO-doped TiO$_2$ to disorder.

© 2017 Acta Materialia Inc. Published by Elsevier Ltd. All rights reserved.

1. Introduction

Titania (TiO$_2$) has excellent electronic and optical properties that enable its applications in photovoltaic, sensing, and a variety of other types of devices (where some levels of low-temperature sintering are often involved) [1–3]. Furthermore, TiO$_2$ has excellent dielectric properties for possible applications in electronics; however, the high sintering temperatures of pure TiO$_2$, which are generally in the range of 1200—1400 °C [4], make it incompatible with the low-temperature co-fired technology [5] that requires the sintering temperature to be appreciably lower than the melting temperature of the metal conductors, such as Cu ($T_m = 1083$ °C) and Ag ($T_m = 961$ °C) [6]. Thus, researchers have made great efforts to lower the sintering temperature of TiO$_2$, e.g., via using mono-disperse TiO$_2$ powder [7] or making sol-gel films [8]. A more common and practical method is to add a small amount of sintering aids to lower the sintering temperature [9]. While CuO is perhaps one of the most effective sintering aid for promoting low-temperature densification of TiO$_2$ [10,11], its exact underlying

mechanisms remain elusive, which motivated this study.

It is well known that CuO doping can reduce the sintering temperatures of TiO$_2$ to ~850—950 °C, which was generally attributed to a liquid-phase sintering effect in prior studies [10,12,13]. However, Lu et al. reported a computed eutectic temperature of 919 °C for the TiO$_2$-CuO system [14]. Recently, de la Rubia et al. suggested that the eutectic temperature is ~1000 °C via differential scanning calorimetry (DSC) and thermogravimetric (TG) analysis, in conjunction with hot-stage microscopy [15]. These results casted doubt on the previously-hypothesized liquid-phase sintering mechanism for CuO-doped TiO$_2$, since the significant densification appeared to occur well below the eutectic temperature, though what is the exact/real eutectic temperature was still controversial prior to this study.

In this study, we conducted careful experiments to unequivocally show that the low-temperature densification of CuO-doped TiO$_2$ is a case of sub-eutectic activated sintering, rather than the commonly-believed liquid-phase sintering. First, we measured the eutectic temperature and composition of the CuO-TiO$_2$ system via calibrating the furnace and characterizing well-quenched specimens. Specifically, we showed that the eutectic reaction takes place between 1000 °C and 1020 °C in air and determined the eutectic

composition to be ~83CuO:17TiO$_2$. Subsequently, we showed that enhanced densification can start below 700–800 °C, well below the bulk eutectic temperature. Furthermore, we observed the stabilization of nanoscale liquid-like intergranular films (IGFs) well below the bulk eutectic temperature by high resolution transmission electron microscopy (HRTEM) and attributed the sub-eutectic activated sintering in CuO-TiO$_2$ to the enhanced mass transport in this nanoscale liquid-like complexion (*a.k.a.* 2-D interfacial phase) that is stabilized below the eutectic temperature at grain boundaries (GBs), analogous those reported previously for Bi$_2$O$_3$-doped ZnO [16] and Ni-doped W and Mo [17–19].

Furthermore, we computed a binary phase diagram for the TiO$_2$-CuO system, which represents a major improvement from (and a correction of) the phase diagram available in literature. Subsequently, a GB λ diagram was also computed to represent the thermodynamic tendency for general GBs in CuO-doped TiO$_2$ to disorder, for the first time for any ceramic system. We adopted an interfacial thermodynamic model to quantitively explain the stabilization of liquid-like IGFs below the bulk eutectic temperature, and to further justify the temperature-dependence of the IGF thicknesses measured by HRTEM.

2. Experiments

To determine the eutectic temperature and composition, rutile-phase TiO$_2$ (99.9+%, purchased from US research Nanomaterials, Inc.) was mixed with CuO powder (99.999%, purchase from Sigma-Aldrich) in a mortar. The mixed powder was uniaxially compressed to pellets at 450 MPa. The surfaces of the pellets were slightly grinded to remove any contamination from the dies. The pellets were then placed in small sapphire crucibles (>99.9% purity, purchased from AdValue Technology), annealed isothermally at desired temperatures (with a heating rate of 5 °C/min before reaching the desired isothermal annealing temperature), and water quenched. Quenched samples were then sectioned, ground, and polished.

Specimens for sintering experiments were made by either a dry mixing or a wet chemistry method. In the dry mixing method, 4 mol. % CuO powder were mixed with rutile-phase TiO$_2$. In the wet chemistry method, an appropriate amount of Cu(NO$_3$)$_2$·2.5H$_2$O (99.99%, purchased from Sigma-Aldrich) was dissolved in DI water to make an aqueous Cu^{2+} solution. Subsequently, rutile TiO$_2$ nanopowder was impregnated in the Cu^{2+} solution. The mixtures were then dried in an oven at 85 °C for 12 h. The dried powders were ground in a mortar for 10 min, followed by annealing in air at 500 °C for 1 h (to decompose Cu(NO$_3$)$_2$ into CuO, which occurs at ~ 180 °C). After annealing, the powders were ground for another 10 min. The final powders (made by either method) were uniaxially pressed at ~200 MPa to make green pellets of 6.35 mm in diameter. The surfaces were slightly ground to remove contamination from the dies. Green densities of the pellets were measured to be ~40%. Linear shrinkages of compacted pellets were measured by a dilatometer (DIL, NETZSCH Group) up to 1000 °C at a constant heating rate of 5 °C/min in air.

In the second batch of sintering experiments, specimens were isothermally sintered in a muffle furnace (Thermolyne Furnace F6000, Thermo Scientific), for which the temperature profile was carefully calibrated using a second thermocouple before the experiments to ensure the accuracy of temperature controls and measurements (for accurately determining the eutectic temperature). This batch of sintered specimens were quenched in water to preserve the high-temperature GB structures for subsequent HRTEM characterization. The densities of specimens were measured using both the weight/dimension and the Archimedes method.

Microstructures and compositions were characterized by a field-emission, ultra-high resolution scanning electron microscope (UHR SEM, FEI XL30) operating at 10 kV, equipped with an Oxford energy-dispersive X-ray spectroscopy (EDS) analyzer. X-ray diffraction (XRD) experiments were conducted using a Rigaku Ultima IV diffractometer (Cu Kα radiation).

Transmission electron microscopy (TEM) samples were prepared using a focused ion beam (FIB, FEI Scios DualBeam). Atomic-level GB structures were characterized by HRTEM using a FEI Titan microscope operating at 300 kV.

3. Results

3.1. Determination of eutectic temperature and composition

SEM images of CuO + 20 mol. % TiO$_2$ specimen (that was a near-eutectic composition selected for the initial experiment *vs.* the actual eutectic composition subsequently measured to be ~83CuO:17TiO$_2$) after annealing at 1020 °C for 0.5 h are shown in Fig. 1; here, a eutectic structure, in which the light-contrast rods were homogeneously embedded in a dark-contrast matrix, can be clearly seen. In contrast, Fig. 2 shows the microstructure and elemental mappings of a CuO + 20 mol. % TiO$_2$ (rutile) specimen after annealed at a slightly lower temperature of 1000 °C for 8 h, where a similar eutectic structure clearly did not form. The corresponding EDS mappings revealed that the light-contrast phase is copper oxide, while the dark-contrast phase is TiO$_2$, with no apparent reaction and virtually no mutual (solid) solubilities. In addition to the SEM images, visual inspection of the specimens also clearly showed the specimen melt at 1020 °C but not at 1000 °C. These results (Fig. 1 *vs.* Fig. 2) undoubtedly suggested that the eutectic temperature of TiO$_2$-CuO is 1010 ± 10 °C.

The XRD patterns of the CuO + 20 mol. % TiO$_2$ specimens quenched from 1000 °C to 1020 °C, respectively, are shown in Fig. 3. Only the two equilibrium CuO and rutile TiO$_2$ phases were detected from specimens that were annealed at 1000 °C for 8 h and water quenched. The CuO + 20 mol. % TiO$_2$ specimen annealed at 1020 °C melted (into a nearly-eutectic liquid so that we did not anneal it longer to prevent the spreading of the liquid and minimize its reaction with the Al$_2$O$_3$ crucible), the non-equilibrium Cu$_2$O and Cu$_3$TiO$_4$ phases, as well as the sapphire Al$_2$O$_3$ impurity phase, were found in the water-quenched specimen (where the crucible was quenched together with the eutectic liquid into the water).

Further quantitative EDS analysis from multiple measurements of the eutectic structures seen in SEM showed the average measured composition corresponded to a cation ratio of Cu:
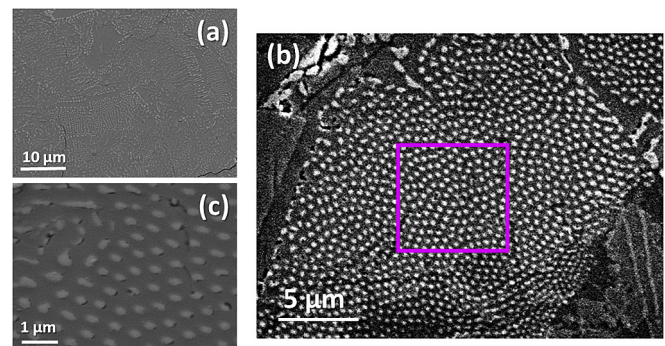

Fig. 1. SEM images of an 80 mol. % CuO + 20 mol. % TiO$_2$ specimen isothermally annealed at 1020 °C for 0.5 h and water-quenched, showing the formation of a eutectic structure. A quantitative composition analysis of the region highlighted in (b) was performed to measure the eutectic composition (to be ~83CuO:17TiO$_2$).
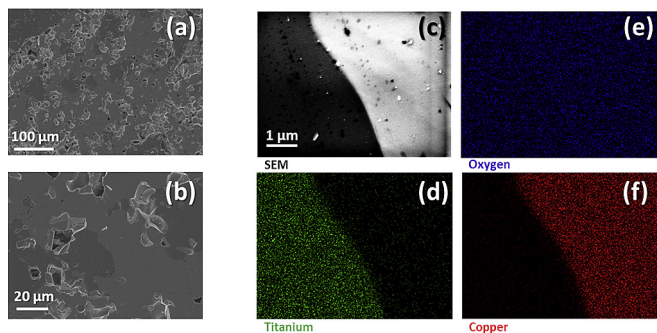
Fig. 2. (a—c) SEM images and (d—f) EDS elemental maps of titanium, copper, and oxygen of an 80 mol. % CuO + 20 mol. % TiO$_2$ specimen that was isothermally annealed at 1000 °C for 8 h and water-quenched, where a eutectic structure is lacking. The specimens were made by a dry mixing route; large particles of CuO remained and the originally-smaller TiO$_2$ particles sintered, whereas no indication of any reaction was evident.

Fig. 4. Linear shrinkage *vs.* temperature curves of pure TiO$_2$ and 4 mol. % CuO-doped TiO$_2$ prepared by two different methods (via wet chemistry and dry mixing routes). All powders were uniaxially pressed at 200 MPa and measured using a dilatometer with a constant ramping rate of 5 °C per minute.

Ti = 4.95 ± 0.11, *i.e.*, the eutectic composition is ~17 mol. % TiO$_2$ + ~83 mol. % CuO.

3.2. Sub-eutectic activated sintering

Fig. 4 shows the linear shrinkage *vs.* temperature curves of undoped and 4 mol. % CuO-doped TiO$_2$ (rutile) measured by dilatometry at a constant heating rate of 5 °C per minute. The doped powders were prepared by either a dry mixing or a wet chemistry method described in the "Experiments" section. At 1000 °C, undoped TiO$_2$ specimen had ~15% linear shrinkage. In contrast, CuO-doped TiO$_2$ specimens had ~32% and ~28% linear shrinkage, respectively, for specimens prepared by the wet chemistry and dry mixing methods, respectively. Both doped TiO$_2$ specimens had ~99% of the theoretical density after the sintering experiments (including possible extra densification during the cooling in the furnace after the dilatometry experiments). These results clearly demonstrated that the addition of CuO effectively promoted the densification of rutile TiO$_2$ below the bulk eutectic temperature, where the significant enhanced densifications occurred at 200—300 °C below the bulk eutectic temperature. The specimen prepared by the wet chemistry method, where the doping was
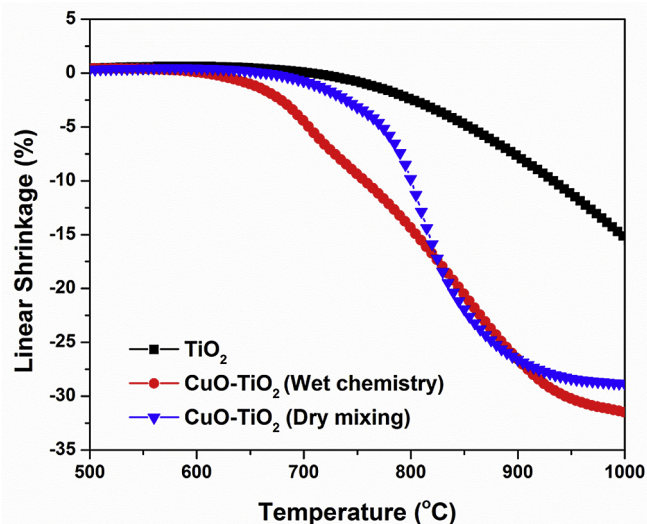
presumably more uniform, exhibited significant enhanced densifications at even lower temperatures (Fig. 4).

To further investigate the sintering mechanism, 4 mol. % CuO-doped TiO$_2$ specimens were isothermally annealed (sintered) at 800 °C, 850 °C, and 900 °C, respectively, for 8 h and subsequently water-quenched. The microstructures of the fractured surfaces of the sintered specimens are shown in Fig. 5 and the measured grain sizes are shown in Fig. 6. Specifically, Fig. 5(a—f) show the SEM images of sintered CuO-doped TiO$_2$ specimens prepared by the wet chemistry method. Low-magnification images show uniform structures and the average grain size increased substantially from 800 °C to 900 °C. Interestingly, a secondary phase (presumably CuO) appeared to wet some triple-grain junctions (with low dihedral angles that, in addition to the nanoscale IGFs at GBs, can also promote sintering and affect microstructural development, as reviewed and discussed by Castro and Gouvêa [20]) of the

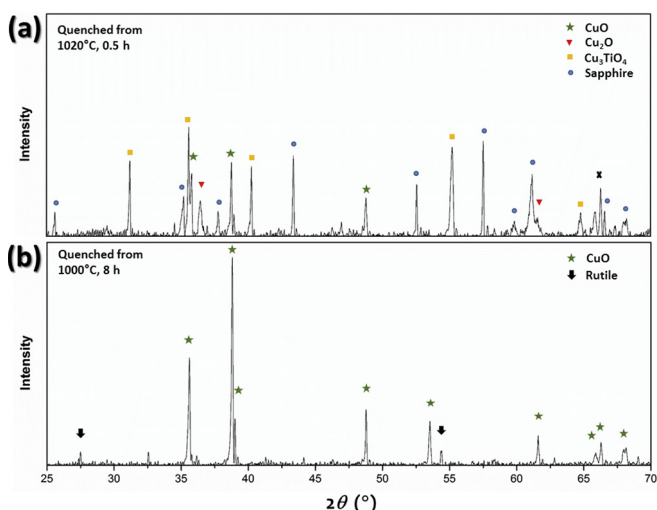**Fig. 3.** X-ray diffraction patterns of 80 mol. % CuO + 20 mol. % TiO$_2$ specimens isothermally annealed and quenched from (a) 1020 °C and (b) 1000 °C, respectively.
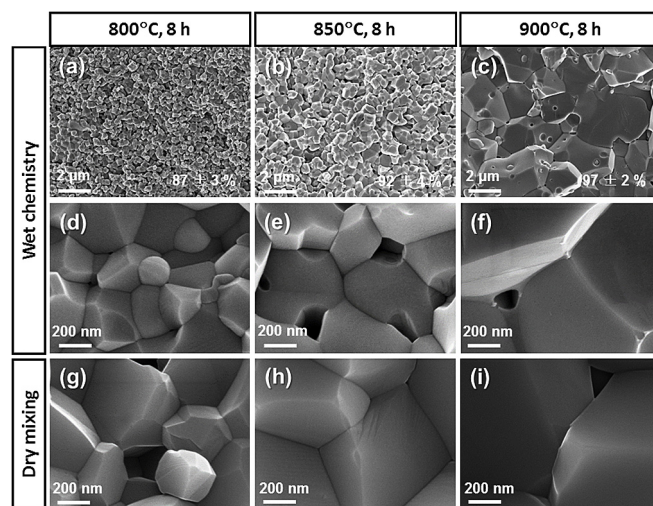

Fig. 5. SEM images of 4 mol. % CuO-doped TiO$_2$ prepared by two different methods via wet chemistry and dry mixing routes, respectively, isothermally annealed at 800 °C, 850 °C, and 900 °C, respectively, for 8 h, and water-quenched.
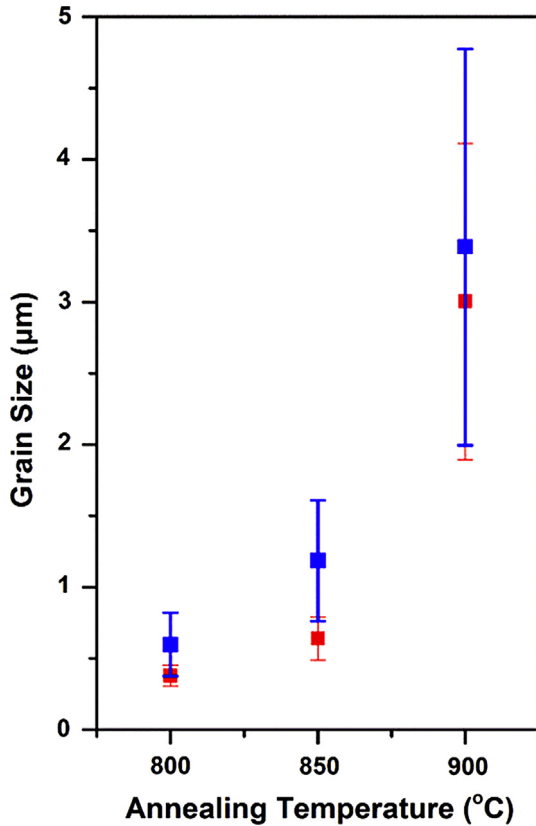
Fig. 6. Measured grain sizes of 4 mol. % CuO-doped TiO₂ specimens, made by the wet chemistry (red) and dry mixing (blue) routes, isothermally annealed at 800 °C, 850 °C, and 900 °C, respectively, for 8 h, and water-quenched. The grain growth behaviors are similar for specimens doped by two different methods. (For interpretation of the references to colour in this figure legend, the reader is referred to the web version of this article.)

specimen sintered and quenched from 900 °C (Fig. 5f), but not in those at lower temperatures. Fig. 5(g–i) display high-magnification SEM images of the CuO-doped TiO₂ prepared by the dry mixing method, sintered at 800 °C, 850 °C, and 900 °C, respectively, for 8 h, and subsequently water quenched. Substantial neck formation and growth were evident in all sub-eutectic sintered specimens (Fig. 5d–i). Finally, we note that the grain growth followed similar trends for the specimens doped by the wet chemistry and dry mixing routes, both of which contained 4 mol. % CuO and were isothermally annealed at 800–900 °C for 8 h (Fig. 6).

3.3. Stabilization of liquid-like GB complexion below the bulk eutectic temperature

Figs. 7 and 8 display the HRTEM images of representative GBs in 4 mol. % CuO-doped TiO₂ specimens that were equilibrated (by isothermal annealing for 8 h) at 800 °C, 850 °C, and 900 °C, respectively, in a calibrated muffle furnace and subsequently water-quenched. In all cases, the GB planes were carefully oriented to be parallel with the incident electron beam to ensure edge-on conditions. Nanometer-thick, structurally-disordered (liquid-like) IGFs were observed in all specimens quenched from 800 °C, 850 °C, and 900 °C after annealing for 8 h, at all GBs that were examined. The measured individual and average thicknesses of the IGFs were listed in Table 1. Specifically, the average measured thickness of the liquid-like IGFs formed at 800 °C (and ± one standard deviation) was 0.70 ± 0.07 nm, which increased to 0.86 ± 0.06 nm for the IGFs

formed at 850 °C and 0.98 ± 0.09 nm for the IGFs formed at 900 °C. These nanoscale IGFs represent a liquid-like interfacial complexion that is thermodynamically stabilized at the general GBs below the bulk eutectic temperature; this stabilization will be quantitively justified by an interfacial thermodynamic model in §4.2 and its roles in activated sintering will be discussed in §4.3.

4. Modeling and discussion

4.1. The TiO₂-CuO binary phase diagram and bulk thermodynamic function

In 2001, a binary TiO₂-CuO phase diagram had been calculated via assuming that the liquid phase is an ideal solution, which produced an eutectic temperature of 919 °C [14], being substantially lower than the ~1000 °C eutectic temperature that was later suggested via DSC and TG analysis in 2012 [15], which is confirmed more directly and accurately by the current study. That diagram reported in 2001 [14] represents the only TiO₂-CuO phase diagram available in literature and has been widely cited. The more accurate measurements of the eutectic temperature and composition obtained in this study, which were consistent with the independent DSC/TG study in 2012 [15], demand a further assessment (and correction) of that TiO₂-CuO phase diagram, which will also provide the thermodynamic function of the liquid phase that will be useful for the interfacial thermodynamic model presented and discussed in the following section.

To compute the binary phase diagram, we assume that CuO and TiO₂ are mutually immiscible in the solid states (since no detectable solid solubility was reported in literature, which was also verified by EDX analysis in the current study) and use the solid phases as the reference state. The free energy of the TiO₂-CuO liquid phase (referenced to the two bulk solid phases) is expressed as a Redlich-Kister polynomial ($n = 0$ and 1 for a subregular solution):

$$\Delta G^{Liq} = X_{CuO}^{Liq} \Delta G_{CuO}^{Liq} + X_{TiO_2}^{Liq} \Delta G_{TiO_2}^{Liq} + RT \left(X_{CuO}^{Liq} ln X_{CuO}^{Liq} + X_{TiO_2}^{Liq} ln X_{TiO_2}^{Liq} \right) + \sum_{n=0,1} L_n \left(X_{CuO}^{Liq} - X_{TiO_2}^{Liq} \right)^n X_{CuO}^{Liq} X_{TiO_2}^{Liq}$$

(1)

where X_i^{Liq} is the bulk molar fraction of the i component ($i =$ CuO, TiO₂) and L_n^{Liq} is the interaction parameters. ΔG_i^{Liq}, the bulk molar fraction and free energy of forming the liquid phase from the solid phase of the i component, can be derived as

$$\Delta G_i^{Liq} = \left(T_i^m - T \right) \Delta S_i^{melt} + \int_{T_i^m}^{T} \Delta C_{P(i)} dT - T \int_{T_i^m}^{T} \frac{\Delta C_{P(i)}}{T} dT$$

(2)

where T_i^m is the melting temperature, ΔS_i^{melt} is the molar entropy of fusion (melting), and $\Delta C_p = C_p^{Liq} - C_p^{Sol}$ is the molar heat capacity difference between solid and liquid phases. For the TiO₂-CuO system, these thermodynamic parameters of individual components (TiO₂ and CuO) were taken from Ref. [14], which were originally obtained from a CRC handbook [21]. Subsequently, we obtained the parameters $L_0 = 8.4$kJ/mol and $L_1 = -13.0$kJ/mol by solving two equations: $\Delta G^{Liq} = 0$ and $\frac{\partial \Delta G^{Liq}}{\partial X_{CuO}} = 0$ to match the experimentally measured eutectic temperature ($T^{Eutectic} = 1010$ °C) and composition ($X_{CuO}^{Eutectic} = 0.832$). Here, the liquid phase is a subregular solution ($L_n = 0$ for $n \geq 2$ in the Redlich-Kister polynomial). From the derived thermodynamic function (Eq. (1)), we calculated the binary (bulk) phase diagram for the TiO₂-CuO system, which is shown in Fig. 9.
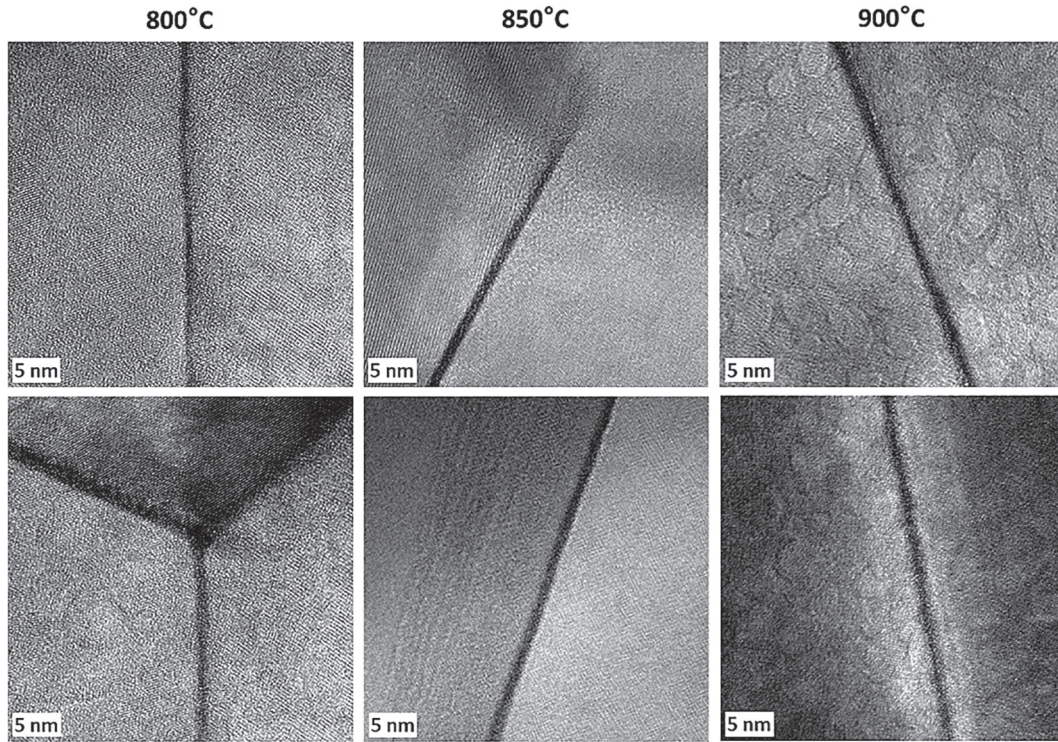
Fig. 7. HRTEM images of 4 mol. % CuO-doped TiO$_2$ specimens isothermally annealed at 800 °C, 850 °C, and 900 °C, respectively, for 8 h and water-quenched.
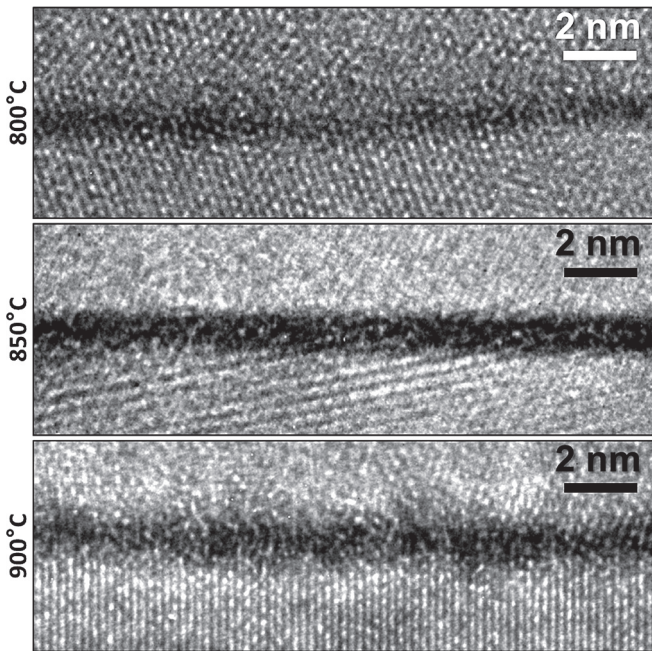

Fig. 8. HRTEM images of 4 mol. % CuO-doped TiO$_2$ specimens equilibrated and quenched at 800 °C, 850 °C, and 900 °C, respectively, at a higher magnification.

We should further note that CuO reduces to Cu$_2$O at 1029 °C in 1-atm air [22] so that the above computation only represents the case that CuO would remain stable at high temperatures (achievable at higher P$_{O2}$). Unfortunately, there is no data available for us to calculate the exact the TiO$_2$-CuO-Cu$_2$O pseudo-binary phase diagram in 1-atm air, but we sketch the possible transitions as the dotted lines in Fig. 9 based on the CuO-to-Cu$_2$O reduction temperature and the melting temperature of Cu$_2$O, which are the only known points in the TiO$_2$-CuO-Cu$_2$O phase diagram. Nonetheless, this CuO-to-Cu$_2$O reduction occurring at 1029 °C should not affect the eutectic reaction at 1010 °C and the stabilization and temperature-dependence of sub-eutectic liquid-like GB complexion (to be discussed in the next section).

4.2. An interfacial thermodynamic model and the computed GB λ diagram

The thermodynamic stability of nanoscale quasi-liquid IGFs (specifically) and GB complexions (in general) have been reviewed [23,24]. Furthermore, GB λ diagrams have been computed and proven useful for predicting trends in activated sintering in (at least) several refractory alloys [25–31]. Here, we made a first successful attempt to extend the prior successes from metallic alloys [25–31] to a ceramic system.

At the length scale of 0.5–5 nm, a phenomenological interfacial

Table 1

Measured IGF thicknesses of 4 mol. % CuO-doped TiO$_2$ specimens equilibrated (isothermally annealed for 8 h) at 800 °C, 850 °C, and 900 °C for 8 h and water-quenched. Three general GBs were measured for each of three specimens. For each of the nine GBs, the IGF thicknesses were measured at 10 different locations; the mean and standard deviations (that represent the uniformities of IGF thicknesses along the individual GBs) were reported.

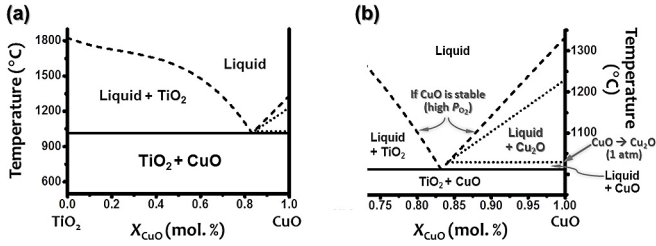| Specimens	800 °C			850 °C			900 °C		
	GB #1	GB #2	GB #3	GB #1	GB #2	GB #3	GB #1	GB #2	GB #3
Measured Thickness of Individual IGFs (nm)	0.68 ± 0.05	0.69 ± 0.04	0.75 ± 0.10	0.89 ± 0.05	0.82 ± 0.07	0.86 ± 0.06	1.01 ± 0.07	0.92 ± 0.07	1.03 ± 0.07
Mean ± 1 Std. Dev. (nm)	0.70 ± 0.07			0.86 ± 0.06			0.98 ± 0.09		

(a)

(b)

Fig. 9. Computed TiO$_2$–CuO phase diagram of (a) the full composition range and (b) an enlarged section of the CuO-rich region. It should be noted that CuO is reduced to Cu$_2$O at 1029°C in air [22] and CuO would remain stable at higher temperatures only at higher P$_{O_2}$. Due to the absence of the Cu$_2$O-TiO$_2$ thermodynamic data, we can only calculate the TiO$_2$–CuO phase diagram. The dotted lines represent the possible transition lines in air with the CuO−Cu$_2$O transformation, while dashed lines represent the calculated phase transformation lines for the TiO$_2$−CuO system assuming no reduction at high temperatures.

thermodynamic model can be formulated for premelting-like IGFs in multicomponent ceramics by combining a sharp-interface model of premelting in unary systems [32] and the Clarke model for equilibrium-thickness IGFs [33,34]. Here, an IGF in the TiO$_2$-CuO is treated as a confined liquid-like interfacial film (*a.k.a.* a specific 2-D interfacial phase) with modified thermodynamic properties. The excess grand potential as a function of the film thickness (h) can be written as:

$$\sigma^x(h) = 2\gamma_{cl} + \Delta G_{amorph}^{(vol)} \cdot h + \sigma_{short-range}(h) + \sigma_{vdW}(h) + \sigma_{elec.}(h) + ..., \tag{3}$$

where γ_{cl} is the crystal-liquid interfacial energy (that is well defined as $h \to +\infty$) and $\Delta G_{amorph}^{(vol)}$ is the volumetric free energy for forming an undercooling liquid from the equilibrium solid phases. The last three terms are short-range, van der Waals (vdW) dispersion, and electrostatic interfacial interactions, which should all vanish as $h \to +\infty$ by definition. A premelting-like GB complexion can be stabilized below the bulk eutectic temperature if the energy penalty for forming an undercooled quasi-liquid film (interfacial phase) of thickness h is overcompensated by the reduction in the total (effective) interfacial energy:

$$-\Delta\gamma \cdot f(h) > \Delta G_{amorph}^{(vol)} h \tag{4}$$

where

$$\Delta\gamma \equiv 2\gamma_{cl} - \sigma^x(0) \tag{5}$$

and $f(h)$ is a dimensionless interfacial coefficient (that varies from $f(0) = 0$ to $f(+\infty) = 1$ by definition, but not necessarily monotonically), defined as:

$$f(h) = 1 + \frac{\left[\sigma_{short-range}(h) + \sigma_{vdW}(h) + \sigma_{elec.}(h) + ...\right]}{\Delta\gamma} \tag{6}$$

The equilibrium thickness, h_{EQ}, corresponds to the minimum of Eq. (3), which implies:

$$\begin{cases} \dfrac{d\sigma^x(h)}{dh}\bigg|_{h=h_{EQ}} = 0 \\[2mm] \dfrac{d^2\sigma^x(h)}{dh^2}\bigg|_{h=h_{EQ}} > 0 \end{cases}. \tag{7}$$

Based on the thermodynamic criterion for stabilizing a sub-eutectic, liquid-like, GB complexion (Eq. (4)), we again adopt

(and, in the next step, quantify) a thermodynamic parameter, λ, to represent the thermodynamic tendency for general GBs to disorder, following earlier studies of metallic alloys [25−31], which is expressed as:

$$\lambda \equiv \frac{-\Delta\gamma}{\Delta G_{amorph}^{(vol)}}, \tag{8}$$

To quantify values of λ, ΔG_{amorph}^{vol}, the volumetric free energy penalty of forming an undercooling liquid below eutectic temperature, is expressed as:

$$\Delta G_{amorph}^{vol} \approx \Delta G_{amorph}^{mol} \Big/ \left[\left(1 - X_{CuO}^{IGF}\right)V_{m(TiO_2)} + X_{CuO}^{IGF}V_{m(CuO)}\right] \tag{9}$$

where X_{CuO}^{IGF} is the average IGF composition and $\Delta G_{amorph}^{mol} = \Delta G^{Liq}(X_{CuO}^{IGF})$, which can be calculated using Eq. (1) and the thermodynamic function and data obtained in the prior section for the TiO$_2$-CuO liquid phase. Here, the most common and convenient way is to select the X_{CuO}^{IGF} that maximizes λ, as discussed in prior studies of metallic alloys [25−31].

To quantify $\Delta\gamma$, $\sigma^x(0) \equiv \gamma_{GB}^{(0)}$, the average general GB energy of pure TiO$_2$ (with no adsorption), was measured in a prior experiment to be 0.87 J/m^2 [35]. Analogous to both a "macroscopic-atoms" model [36,37] and a lattice model [38] (with modifications), we estimate the average interfacial energy for the crystal-liquid interface between a pure TiO$_2$ solid and a TiO$_2$-CuO binary liquid using the following expression:

$$\gamma_{cl} = \frac{\Delta H_{TiO_2}^{melt}}{\kappa m_1^{-1} V_m^{2/3}} + \frac{\Omega_{CuO-TiO_2}^{Liq}}{\kappa m_1^{-1} V_m^{2/3}}\left(X_{CuO}^{IGF}\right)^2, \tag{10}$$

where the two terms represent the enthalpic (fusion) and chemical (interaction) contributions, respectively, to the crystal-liquid interfacial energy. Here, $\Delta H_{TiO_2}^{melt}$ is the molar enthalpy (latent heat) of melting, $\Omega_{CuO-TiO_2}^{Liq} = L_0$ is the regular-solution parameter for the liquid phase, V_m is the molar volume of TiO$_2$, κ is a geometric factor ($\kappa \equiv A_m/V_m^{2/3}$, where A_m is the area of 1 mol of molecules spread as a monolayer [38]), and m_1 is the fraction of bonds across the crystal-liquid interface. The value of κm_1^{-1} in Eq. (10) depends on the lattice structure and orientation of the interface and we use $\kappa m_1^{-1} = C_0 \approx 4.5 \times 10^8$ to represent the average of different orientations [39] to represent IGFs formed at the average general GBs.

Subsequently, we computed λ values and plotted them in the bulk TiO$_2$-CuO phase diagram to construct a GB λ diagram for CuO-doped TiO$_2$, as shown in Fig. 10, similar to the GB λ diagrams constructed in prior studies for several metallic alloys [25−31]. In the sub-eutectic two-phase region, the computed λ increases with increasing temperature, suggesting increasing thermodynamic tendency for average general GBs to disorder that should result in increasing densification rates, consistent with both the intuition and experiments.

A more rigorous and accurate assessment of IGF thickness (h_{EQ}) *vs.* temperature requires the quantitative information about the short-range, vdW dispersion, electrostatic, and any other interfacial interactions in Eq. (3), which is unfortunately not available for the current case of TiO$_2$-CuO as well as virtually all other ceramic systems. However, we may adopt a simplified model to justify the observed temperature-dependent IGF thicknesses in the intermediate temperature region (to be defined and discussed subsequently), as follows. First, prior analyses showed that the vdW dispersion interaction, which is always attractive for the IGFs, will be overwhelmed by the ΔG_{amorph}^{vol} term that represents a significantly higher attractive pressure than the vdW dispersion pressure at $\Delta T \equiv T - T^{Eutectic} \geq 100$ °C [24,40]; thus, the vdW dispersion
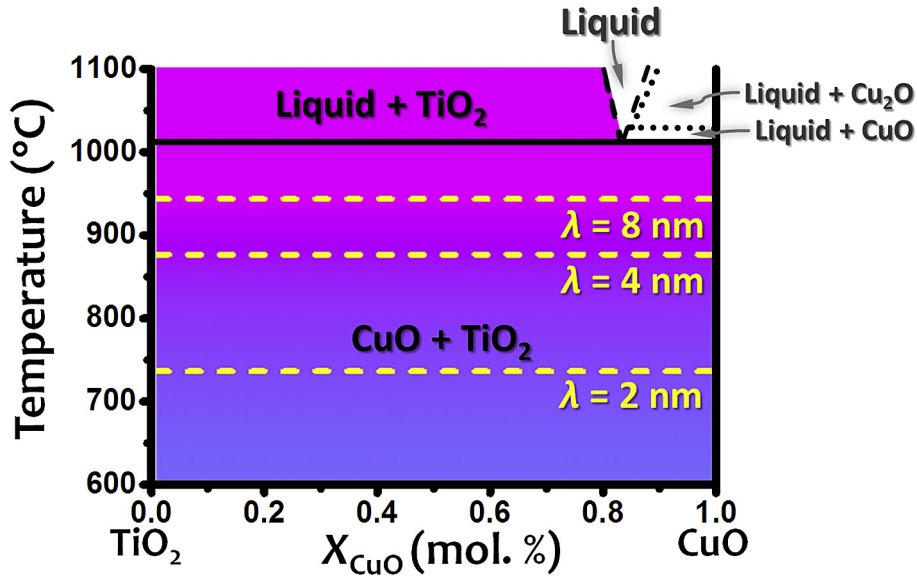
Fig. 10. A computed GB λ diagram, where the dash lines represent $\lambda = 2$ nm, 4 nm, and 8 nm, respectively, and the color represent the relative thermodynamic tendency for the average general GBs in CuO-doped TiO$_2$ to disorder.

interaction can be neglected well below the eutectic temperature. Moreover, either the short-range or electrostatic interaction can be approximated with an exponentially-decaying form (and only one of them likely dominates in a specific ceramic system). Thus, in a simplified model, we can adopt an exponentially-decaying interfacial potential, $f(h) = 1 - \exp(-h/\xi)$, so that Eq. (3) can be rewritten and simplified to:

$$\Delta\sigma(h) \equiv \sigma^x(h) - \sigma^x(0) = \Delta\gamma \cdot f(h) + \Delta G_{amorph}^{(vol)} \cdot h$$
$$= \Delta\gamma \cdot [1 - \exp(-h/\xi)] + \Delta G_{amorph}^{(vol)} \cdot h, \quad (11a)$$

where ξ is a coherent length [27]. Eq. (11a) can also be rewritten into a dimensionless form:

$$\frac{\Delta\sigma(h)}{-\Delta\gamma} = \frac{h}{\lambda} + \exp(-h/\xi) - 1. \quad (11b)$$

Minimizing Eq. (11b) with respective to h produces the equilibrium IGF thickness:

$$h_{EQ} = \xi \ln(\lambda/\xi). \quad (12)$$

We should further make two notes. First, Eq. (12) is obtained via assuming a fixed average film composition that maximizes λ in Eq. (8). Alternatively, we may minimize Eq. (11a) with respective to both h and X_{CuO}^{IGF}. Our numerical analysis showed negligible differences between the calculated "h_{EQ} vs. T" curves using the two approaches so we choose the simpler approach [by using Eq. (12)]. Second, this simplified model [Eq. (11) and Eq. (12)] can only be used for the intermediate temperature region. On one hand, at higher temperatures ($T \sim T^{Eutectic}$), the divergence of h_{EQ} predicted from this model should be limited by the attractive vdW dispersion interaction. On the other hand, at lower temperatures, this continuum model is no longer valid when $h_{EQ} < \sim 0.5$ nm because it does not consider the discrete nature of ion sizes and bond lengths. Nonetheless, this simplified model can be used to justified the measured temperature-dependent IGF thicknesses in the intermediate temperature region of 800—900 °C for the current case, which is the range of interest for activated sintering.

Specifically, Fig. 11 plots the means and standard deviations of IGF thicknesses measured by HRTEM from specimens equilibrated at 800 °C, 850 °C, and 900 °C, along with the computed "h_{EQ} vs. T" curves for three different selections of the coherent length, ξ. The computed "h_{EQ} vs. T" curve with $\xi = 0.38$ nm produced the best fit to the experimental data, while the sensitivity of the different selections of ξ was also tested. Although we do not have the knowledge of the exact value of the coherent length, the value that produced the best fit (~0.38 nm) is about twice of the O-Cu bond length or the size of a Cu-O$_n$ polyhedral unit, which appears to be reasonable. Thus, this rather simplified model can justify the stabilization of liquid-like GB complexions below the eutectic temperature as well as the temperature-dependent interfacial widths (the measured "h_{EQ} vs. T") observed by HRTEM.
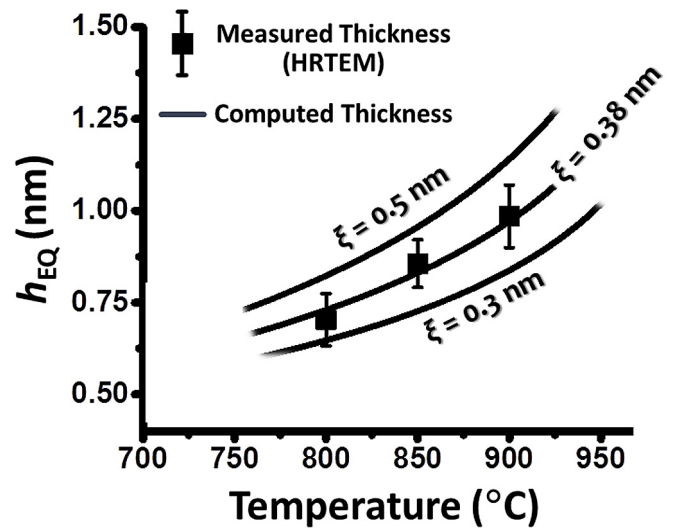

Fig. 11. The average IGF thicknesses vs. equilibration temperatures measured by HRTEM. The three solid lines represent the computed equilibrium thickness (h_{EQ}) as functions of temperature with three different coherence lengths ($\xi = 0.3$ nm, 0.38 nm, and 0.5 nm, respectively, where $\xi = 0.38$ nm represents the best fit with the experimental data).

Lastly, we should also recognize the possibility that some of these IGFs exhibit discrete (instead of continuous) thickness (to form Dillon-Harmer GB complexions [23,41]) for certain specific GBs, e.g., some special GBs with low-index grain surfaces, as shown in a prior study for a (001)//(100) GB in a ($CuO + SiO_2$) doped TiO_2 bicrystal specimen [41]. The origin of the discrete thicknesses and the formation of Dillon-Harmer GB complexions can be explained in the same interfacial thermodynamic framework discussed above via incorporating (adding) an oscillatory structural interaction (as a result of a fixed, finite, atomic size using a hard-sphere approximation) in Eq. (3) or the interfacial coefficient $f(h)$ [31,41–43].

4.3. Further discussion of activated sintering mechanisms and beyond

The current study measured the eutectic temperature of the TiO_2-CuO system to be $1010 \pm 10\,°C$ in air, which was higher than that reported in 2001 [14], but similar to that suggested by a DSC and TG study in 2012 [15]. This warrantees our re-assessment and a correction of the TiO_2-CuO phase diagram reported in Ref. [14] in 2001 based on our measured bulk eutectic temperature and composition to compute an improved (corrected) TiO_2-CuO phase diagram in Fig. 9; this assessment also provided the thermodynamic function for justifying the stabilization of a sub-eutectic liquid-like GB complexion, which leads to enhanced interfacial mass transport and subsequently activated sintering.

The combination of our experimental results undoubtedly demonstrated that the enhanced sintering of CuO-doped TiO_2 occurred in the sub-eutectic region, starting at $>300\,°C$ below the bulk eutectic temperature. Thus, this study clearly disapproved the theory that the enhanced sintering in CuO-doped TiO_2 at ~850–950 °C is due to liquid-phase sintering, that was widely assumed in prior studies [10,12,13]. Instead, this study strongly suggested, via a combination of HRTEM and thermodynamic modeling, that the addition of CuO promoted the formation of a liquid-like GB complexion in TiO_2 well below the bulk eutectic temperature, which provides a fast mass transport pathway to enhance sub-eutectic densification. After completing all of our experimental and modeling work, we noticed a most-recently published independent study by Paek et al. [44] during the final revision of our manuscript, where the authors also found similar nanoscale IGFs in CuO-doped TiO_2 in the temperature range of 850–950 °C and proposed a similar low-temperature sintering mechanism (without quantitative modeling) [44]. Similar solid-state activated sintering behaviors and mechanisms have also been observed/identified for several ceramic (Bi_2O_3-doped ZnO [16]) and metallic (Ni-doped W and Mo [17–19]) systems.

We should recognize that observing the formation of premelting like IGFs (Figs. 7 and 8) at the same temperature range of sub-eutectic activated sintering (Figs. 4 and 5) is a very strong suggestion, yet not a direct proof, of the proposed mechanism of enhanced sintering in CuO-doped TiO_2. Thus, we should further discuss alternative mechanisms that may enhance sintering below the eutectic temperatures. Specifically, a recent study by Wu, Dholabhai, Uberuaga, and Castro showed that the reduction of Mn cations from 3+ to 2+ in Mn-doped CeO_2 can result in significant coarsening [45]. In Mn-doped CeO_2, Mn inhibited grain growth/coarsening below 800 °C and this inhibition effect became ineffective at $>800\,°C$ due to reduction of Mn [45]. In the current study, adding CuO promoted sintering at all temperatures (~600–1000 °C) as compared with pure TiO_2 (Fig. 4) with only moderate (not discontinuous) grain growth/coarsening (Fig. 6); thus, the same mechanism proposed for Mn-doped CeO_2 cannot apply directly. Yet, we recognize other possible doping or reduction effects that

change the defect concentrations either at interfaces or in the bulk phase, which may subsequently change the sintering rates by changing the bulk or interfacial ion/mass transport rates. In the current case, CuO can be reduced to Cu_2O at ~1029 °C [22] (with some partial reduction starts at ~1000 °C in the CuO-TiO_2 binary system as shown in an earlier study [15]), whereas the enhanced densification occurred at much lower temperatures (as low as 700–900 °C; Figs. 4 and 5). Thus, it is unlikely that the reduction of CuO played a major role in enhancing sintering at sub-eutectic temperatures (~700–1000 °C) in the current case of CuO-doped TiO_2.

Moreover, IGFs should form quickly enough to enable the promotion of densification in the initial stage of sintering, which is possible due to the typical fast surface and GB diffusion rates at such temperatures; this is even easier to be realized in specimens prepared by the wet chemistry route where CuO could spread on the surfaces of TiO_2 particles upon annealing at 500 °C, similar to those demonstrated in various supported (monolayer) oxide catalysts and other (nanoscale) surface phases [46–49]. Specifically, a most-recently published independent study by Paek et al. [44] also showed the formation of IGFs in earlier stages (e.g., after annealing at 850 °C for 1 h) in CuO-doped TiO_2. The time that is needed for forming IGFs, which presumably enhance sintering subsequently, can also explain the observed result that the densification rates in specimen prepared by the wet chemistry route were higher than those made by the dry mixing method at low temperatures (particularly in ~650–800 °C, as shown in Fig. 4).

The thermodynamic stabilization of nanometer-thick quasi-liquid IGFs below eutectic temperature in CuO-doped TiO_2 has been well-justified by estimating relative interfacial energies via both experimental data and a statistical model as well as quantifying free-energy penalty for forming undercooled liquids using CAL-PHAD data. Subsequently, an interfacial thermodynamic model is used to justify the temperature-dependent interfacial width.

Following the earlier successes of constructing GB λ diagrams to predict useful trends in high-temperature GB disordering and to subsequently forecast activated sintering behaviors (and potentially other materials properties such as creep resistance) in several W- and Mo based metallic alloys [25–31] (as well as more rigorous computed GB complexion diagrams with well-defined transition lines, such as that for Bi-doped Ni in a most recent report [50]), this study made a first successful attempt to extend the model and method to compute the first GB λ diagram for a ceramic system (CuO-doped TiO_2). In future studies, similar or more rigorous "GB diagrams" should be developed for other ceramic systems, which can have broad applications. This is in part because this class of nanoscale IGFs are more ubiquitous and technologically-important for ceramics than metals in general. Furthermore, it is worth noting that nanometer-thick IGFs investigated in this study only represent one of several types of GB complexions discovered recently [23,51–53]; such GB complexions (a.k.a. interfacial phases that are thermodynamically 2-D) exist ubiquitously in both metallic and ceramic materials, where they can often critically influence or even control a board range of transport, mechanical, and physical properties [23,25,27,43,51,54–71] beyond sintering.

5. Conclusions

The eutectic temperature of the CuO-TiO_2 system has been determined to be $1010 \pm 10\,°C$ and the eutectic composition was measured to be ~$17TiO_2$:$83CuO$ (or ~17 mol. % TiO_2 + ~83 mol. % CuO). Based on the measured eutectic temperature and composition, we computed the binary TiO_2-CuO phase diagram (representing a significant improvement from, and essentially a correction of, the phase diagram available in literature) and

formulated the relevant thermodynamic function. A combination of dilatometry measurements and isothermal sintering experiments unequivocally demonstrated the occurrence of activated sintering in CuO-doped TiO_2 at as low as >300 °C below the bulk eutectic temperature. HRTEM characterization of well-quenched specimens further revealed the formation of nanometer-thick, liquid-like IGFs. It is likely that the enhanced mass transport in this premelting-like complexion can result in the sub-eutectic activated (enhanced) sintering observed in this system. We further calculated a GB λ diagram, for the first time for any ceramic system, to represent the thermodynamic tendency for general GBs in CuO-doped TiO_2 to disorder and used an interfacial thermodynamic model to quantitively explain and justify the stabilization of nanometer-thick, liquid-like IGFs below the bulk eutectic temperature as well as the temperature-dependent IGF thicknesses measured by HRTEM. In future studies, similar or different (more rigorous and sophisticated) types of GB diagrams should be computed for other ceramic materials, which can potentially have broad scientific and technological impacts.

References

[1] M. Gratzel, Photoelectrochemical cells, Nature 414 (6861) (2001) 338–344.
[2] R. Asahi, T. Morikawa, T. Ohwaki, K. Aoki, Y. Taga, Visible-light photocatalysis in nitrogen-doped titanium oxides, Science 293 (5528) (2001) 269–271.
[3] X. Chen, S.S. Mao, Titanium dioxide nanomaterials: synthesis, properties, modifications, and applications, Chem. Rev. 107 (7) (2007) 2891–2959.
[4] F.M. Meng, Influence of sintering temperature on semi-conductivity and nonlinear electrical properties of TiO_2-based varistor ceramics, Mater. Sci. Eng. B Solid State Mater. Adv. Technol. 117 (1) (2005) 77–80.
[5] L. Golonka, Technology and applications of low temperature cofired ceramic (LTCC) based sensors and microsystems, Bull. Pol. Acad. Sci. Tech. Sci. 54 (2) (2006).
[6] M.T. Sebastian, H. Jantunen, Low loss dielectric materials for LTCC applications: a review, Int. Mater. Rev. 53 (2) (2008) 57–90.
[7] E.A. Barringer, H.K. Bowen, Formation, packing, and sintering of monodisperse TiO_2 powders, J. Am. Ceram. Soc. 65 (12) (1982) C199–C201.
[8] K.N.P. Kumar, K. Keizer, A.J. Burggraaf, T. Okubo, H. Nagamoto, S. Morooka, Densification of nanostructured titania assisted by a phase-transformation, Nature 358 (6381) (1992) 48–51.
[9] S.-H. Yoon, D.-W. Kim, S.-Y. Cho, K.S. Hong, Phase analysis and microwave dielectric properties of LTCC TiO_2 with glass system, J. Eur. Ceram. Soc. 23 (14) (2003) 2549–2552.
[10] J.C. Chang, Y.F. Chen, J.H. Jean, Low-fire processing and dielectric properties of TiO_2 with MnOx-CuO, Jpn. J. Appl. Phys. Part 1 Regular Pap. Short Notes Rev. Pap. 43 (7A) (2004) 4267–4268.
[11] M. Valant, D. Suvorov, R.C. Pullar, K. Sarma, N.M. Alford, A mechanism for low-temperature sintering, J. Eur. Ceram. Soc. 26 (13) (2006) 2777–2783.
[12] D.W. Kim, T.G. Kim, K.S. Hong, Low-firing of CuO-doped anatase, Mater. Res. Bull. 34 (5) (1999) 771–781.
[13] D.W. Kim, B. Park, J.H. Chung, K.S. Hong, Mixture behavior and microwave dielectric properties in the low-fired TiO_2-CuO system, Jpn. J. Appl. Phys. Part 1 Regular Pap. Short Notes Rev. Pap. 39 (5A) (2000) 2696–2700.
[14] F.H. Lu, F.X. Fang, Y.S. Chen, Eutectic reaction between copper oxide and titanium dioxide, J. Eur. Ceram. Soc. 21 (8) (2001) 1093–1099.
[15] M.A. de la Rubia, J.J. Reinosa, P. Leret, J.J. Romero, J. de Frutos, J.F. Fernandez, Experimental determination of the eutectic temperature in air of the CuO-TiO_2 pseudobinary system, J. Eur. Ceram. Soc. 32 (1) (2012) 71–76.
[16] J. Luo, H.F. Wang, Y.M. Chiang, Origin of solid-state activated sintering in Bi_2O_3-doped ZnO, J. Am. Ceram. Soc. 82 (4) (1999) 916–920.
[17] X. Shi, J. Luo, Grain boundary wetting and prewetting in Ni-doped Mo, Appl. Phys. Lett. 94 (25) (2009) 251908.
[18] V.K. Gupta, D.H. Yoon, H.M. Meyer III, J. Luo, Thin intergranular films and solid-state activated sintering in nickel-doped tungsten, Acta Mater 55 (2007) 3131–3142.
[19] J. Luo, V.K. Gupta, D.H. Yoon, H.M. Meyer, Segregation-induced grain boundary premelting in nickel-doped tungsten, Appl. Phys. Lett. 87 (2005) 231902.
[20] R.H. Castro, D. Gouvêa, Sintering and nanostability: the thermodynamic perspective, J. Am. Ceram. Soc. 99 (4) (2016) 1105–1121.
[21] J.F. Shackelford, Y.-H. Han, S. Kim, S.-H. Kwon, CRC Materials Science and Engineering Handbook, CRC press, 2016.
[22] H. Nishiura, R.O. Suzuki, K. Ono, L.J. Gauckler, Experimental phase diagram in the Ag-Cu_2O-CuO system, J. Am. Ceram. Soc. 81 (8) (1998) 2181–2187.
[23] P.R. Cantwell, M. Tang, S.J. Dillon, J. Luo, G.S. Rohrer, M.P. Harmer, Overview No. 152: grain boundary complexions, Acta Mater 62 (2014) 1–48.
[24] J. Luo, Stabilization of nanoscale quasi-liquid interfacial films in inorganic materials: a review and critical assessment, Crit. Rev. Solid State Mater. Sci. 32 (1–2) (2007) 67–109.
[25] N. Zhou, T. Hu, J. Luo, Grain boundary complexions in multicomponent alloys: challenges and opportunities, Curr. Opin. Solid State Mater. Sci. 20 (2016) 268–277.
[26] N. Zhou, J. Luo, Developing grain boundary diagrams for multicomponent alloys, Acta Mater 91 (2015) 202–216.
[27] J. Luo, Developing interfacial phase diagrams for applications in activated sintering and beyond: current status and future directions, J. Am. Ceram. Soc. 95 (8) (2012) 2358–2371.
[28] X. Shi, J. Luo, Developing grain boundary diagrams as a materials science tool: a case study of nickel-doped molybdenum, Phys. Rev. B 84 (1) (2011) 014105.
[29] X. Shi, J. Luo, Decreasing the grain boundary diffusivity in binary alloys with increasing temperature, Phys. Rev. Lett. 105 (2010) 236102.
[30] J. Luo, X.M. Shi, Grain boundary disordering in binary alloys, Appl. Phys. Lett. 92 (2008) 101901.
[31] J. Luo, Liquid-like interface complexion: from activated sintering to grain boundary diagrams, Curr. Opin. Solid State Mater. Sci. 12 (5/6) (2008) 81–88.
[32] J.G. Dash, A.M. Rempel, J.S. Wettlaufer, The physics of premelted ice and its geophysical consequences, Rev. Mod. Phys. 78 (2006) 695–741.
[33] D.R. Clarke, T.M. Shaw, A.P. Philipse, R.G. Horn, Possible electrical double-layer contribution to the equilibrium thickness of intergranular glass films in polycrystalline ceramics, J. Am. Ceram. Soc. 76 (1993) 1201–1204.
[34] D.R. Clarke, On the equilibrium thickness of intergranular glass phases in ceramic materials, J. Am. Ceram. Soc. 70 (1) (1987) 15–22.
[35] R.H.R. Castro, B.B. Wang, The hidden effect of interface energies in the polymorphic stability of nanocrystalline titanium dioxide, J. Am. Ceram. Soc. 94 (3) (2011) 918–924.
[36] L.P.H. Jeurgens, Z. Wang, E.J. Mittemeijer, Thermodynamics of reactions and phase transformations at interfaces and surfaces, Int. J. Mater. Res. 100 (10) (2009) 1281–1307.
[37] R. Benedictus, A. Böttger, E.J. Mittemeijer, Thermodynamic model for solid-state amorphization in binary systems at interfaces and grain boundaries, Phys. Rev. B 54 (13) (1996) 9109–9125.
[38] N. Eustathopoulos, M. Nicholas, B. Drevet, Wettability at High Temperatures, Pergamon, Amsterdam, 1999.
[39] H. Bakker, Enthalpies in Alloys, Miedema's Semi-empirical Model, Trans. Tech. Publications, 1998, pp. 1–78.
[40] J. Luo, Y.-M. Chiang, Existence and stability of nanometer-thick disordered films on oxide surfaces, Acta Mater 48 (18–19) (2000) 4501–4515.
[41] S. Ma, P.R. Cantwell, T.J. Pennycook, N. Zhou, M.P. Oxley, D.N. Leonard, S.J. Pennycook, J. Luo, M.P. Harmer, Grain boundary complexion transitions in WO_3- and CuO-doped TiO_2 bicrystals, Acta Mater 61 (5) (2013) 1691–1704.
[42] J. Luo, Grain boundary complexions: the interplay of premelting, prewetting, and multilayer adsorption, Appl. Phys. Lett. 95 (7) (2009) 071911.
[43] S.J. Dillon, M.P. Harmer, J. Luo, Grain boundary complexions in ceramics and metals: an overview, JOM 61 (12) (2009) 38–41.
[44] Y.-K. Paek, C.-K. Shin, K.-S. Oh, T.-J. Chung, H.J. Cho, Low-temperature sintering behavior of TiO_2 activated with CuO, J. Korean Ceram. Soc. 53 (6) (2016) 682–688.
[45] L. Wu, P.P. Dholabhai, B.P. Uberuaga, R.H. Castro, Temperature dependence discontinuity in the stability of manganese doped ceria nanocrystals, Cryst. Growth Des. 17 (2017) 446–453.
[46] Y.-C. Xie, Y.-Q. Tang, Spontaneous monolayer dispersion of oxides and salts onto surfaces of supports: applications to heterogeneous catalysis, Adv. Catal. 31 (1990) 1–43.
[47] H. Qian, J. Luo, Nanoscale surficial films and a surface transition in V_2O_5-TiO_2-based ternary oxide systems, Acta Mater 56 (2008) 4702–4714.
[48] H.J. Qian, J. Luo, Vanadia-based equilibrium-thickness amorphous films on anatase (101) surfaces, Appl. Phys. Lett. 91 (6) (2007) 061909.
[49] J. Luo, Y.-M. Chiang, Wetting and prewetting on ceramic surfaces, Annu. Rev. Mater. Res. 38 (2008) 227–249.
[50] N. Zhou, Z. Yu, Y. Zhang, M.P. Harmer, J. Luo, Calculation and validation of a grain boundary complexion diagram for Bi-doped Ni, Scr. Mater. 130 (2017) 165–169.
[51] W.D. Kaplan, D. Chatain, P. Wynblatt, W.C. Carter, A review of wetting versus adsorption, complexions, and related phenomena: the rosetta stone of wetting, J. Mater. Sci. 48 (2013) 5681–5717.
[52] S.J. Dillon, M. Tang, W.C. Carter, M.P. Harmer, Complexion: a new concept for kinetic engineering in materials science, Acta Mater 55 (18) (2007) 6208–6218.
[53] S. Ma, K. Meshinchi Asl, C. Tansarawiput, P.R. Cantwella, M. Qi, M.P. Harmer, J. Luo, A grain-boundary phase transition in Si-Au, Scr. Mater. 66 (2012) 203–206.
[54] J. Luo, A short review of high-temperature wetting and complexion transitions with a critical assessment of their influence on liquid metal

embrittlement and corrosion, Corrosion 72 (7) (2015) 897–910.

[55] J. Luo, Interfacial engineering of solid electrolytes, J. Materiomics 1 (1) (2015) 22–32.

[56] J. Luo, H. Cheng, K.M. Asl, C.J. Kiely, M.P. Harmer, The role of a bilayer interfacial phase on liquid metal embrittlement, Science 333 (6050) (2011) 1730–1733.

[57] A. Khalajhedayati, Z. Pan, T.J. Rupert, Manipulating the interfacial structure of nanomaterials to achieve a unique combination of strength and ductility, Nat. Commun. 7 (2016) 10802.

[58] A. Tewari, P. Bowen, Grain boundary complexion and transparent polycrystalline alumina from an atomistic simulation perspective, Curr. Opin. Solid State Mater. Sci. 20 (5) (2016) 278–285.

[59] B.B. Straumal, A.A. Mazilkin, B. Baretzky, Grain boundary complexions and pseudopartial wetting, Curr. Opin. Solid State Mater. Sci. 20 (5) (2016) 247–256.

[60] O. Schumacher, C.J. Marvel, M.N. Kelly, P.R. Cantwell, R.P. Vinci, J.M. Rickman, G.S. Rohrer, M.P. Harmer, Complexion time-temperature-transformation (TTT) diagrams: opportunities and challenges, Curr. Opin. Solid State Mater. Sci. 20 (5) (2016) 316–323.

[61] T.J. Rupert, The role of complexions in metallic nano-grain stability and deformation, Curr. Opin. Solid State Mater. Sci. 20 (5) (2016) 257–267.

[62] G.S. Rohrer, The role of grain boundary energy in grain boundary complexion transitions, Curr. Opin. Solid State Mater. Sci. 20 (5) (2016) 231–239.

[63] J.M. Rickman, J. Luo, Layering transitions at grain boundaries, Curr. Opin. Solid State Mater. Sci. 20 (5) (2016) 225–230.

[64] W. Rheinheimer, M.J. Hoffmann, Grain growth in perovskites: what is the impact of boundary transitions? Curr. Opin. Solid State Mater. Sci. 20 (5) (2016) 286–298.

[65] S.A.E. Johansson, G. Wahnström, First-principles derived complexion diagrams for phase boundaries in doped cemented carbides, Curr. Opin. Solid State Mater. Sci. 20 (5) (2016) 299–307.

[66] Q. Gao, M. Widom, Surface and grain boundary complexions in transition metal – bismuth alloys, Curr. Opin. Solid State Mater. Sci. 20 (5) (2016) 240–246.

[67] T. Frolov, M. Asta, Y. Mishin, Phase transformations at interfaces: observations from atomistic modeling, Curr. Opin. Solid State Mater. Sci. 20 (5) (2016) 308–315.

[68] S.J. Dillon, K. Tai, S. Chen, The importance of grain boundary complexions in affecting physical properties of polycrystals, Curr. Opin. Solid State Mater. Sci. 20 (5) (2016) 324–335.

[69] G.S. Rohrer, M.P. Martin, Grain boundary complexions – current status and future directions, Curr. Opin. Solid State Mater. Sci. 20 (5) (2016) (iv-v).

[70] B.B. Straumal, B. Baretzky, Grain boundary phase transitions and their influence on properties of polycrystals, Interf. Sci. 12 (2004) 147–155.

[71] A. Kundu, K.M. Asl, J. Luo, M.P. Harmer, Identification of a bilayer grain boundary complexion in Bi-doped Cu, Scr. Mater. 68 (2013) 146–149.